

# Topological classification for intersection singularities of exceptional surfaces in pseudo-Hermitian systems

Hongwei Jia<sup>#</sup>, Ruo-Yang Zhang<sup>#</sup>, Jing Hu, Yixin Xiao, Zhao-Qing Zhang, Yifei Zhu<sup>\*</sup>, C. T. Chan<sup>†</sup>

**Abstract:** Exceptional degeneracy plays a pivotal role in the topology of non-Hermitian systems, and recently many efforts have been devoted to classifying exceptional points and exploring the intriguing physics. However, intersections of exceptional surfaces, which are commonly present in non-Hermitian systems with parity-time symmetry or chiral symmetry, were not classified. Here we classify a generic pseudo-Hermitian system, for which the momentum space is partitioned by exceptional surfaces, and these surface intersections are stable to perturbations to the Hamiltonian. By constructing the quotient space with equivalence relations of eigenstates, we reveal that the topology of such gapless structure can be described by a free non-Abelian group composed of products of two generators. The topological invariants in the group are associated with the polarization conversion of eigenstates via adiabatic transformations. Our classification does not rely on specific bandgaps and is thus a global topological description. Importantly, the classification predicts a new phase of matter, and can systematically explain how the exceptional surfaces and their intersections evolve against perturbations to the Hamiltonian. Our work opens a new pathway for designing systems with robust topological phases, and is potentially a guidance for applications to sensing and lasing devices utilizing exceptional surfaces and intersections.

**Introduction:** Singularities, characterized by the property of non-differentiability, are ubiquitous and play important roles in physics of many systems in the real world. The occurrence of a singularity is always accompanied with exotic physical phenomena [1,2,3,4,5,6,7,8,9,10,11,12,13]. As a prime example, a Weyl point in Hermitian systems acts as a sink or source of the Berry curvature, and the Fermi-arc surface state links two Weyl points with opposite chiralities [1,2,9,11]. A pivotal way for understanding singularities is topology. A singularity can be characterized by a topological invariant (e.g., Chern number), which can be calculated with the adiabatic evolution of eigenstates on loops/surfaces enclosing the singularity [5,6,7,8,9,11]. Recently, the topology of non-Hermitian systems is attracting growing attention [14,15,16,17,18,19,20,21,22,23,24]. Non-Hermiticity is ubiquitous because most systems are not isolated. The eigenenergies become complex, representing energy exchange with surrounding environment. The exceptional point, defined on complex energy plane, is thus a unique feature of non-Hermiticity, and is a singular point where both the eigenenergies and the eigenstates coalesce [14,15,16,18,19]. Different from Weyl points and nodal lines in Hermitian systems, the exceptional point carries fractional topological invariants [16,18,19,24], and can induce the stable bulk Fermi-arcs [22,24]. The skin effect in open boundary systems, is associated with the bulk topology in point gaps [15,16,17,18,21,23]. Recent discoveries of lines, rings and surfaces of exceptional points further enriched the topological classes [25,26,27,28,29]. High-order exceptional degeneracies, which are often present as intersections or cusps of exceptional lines/surfaces, carry hybrid topological invariants [30].

Lots of efforts have been devoted to classifying exceptional points recently. Topological classifications are important, because whenever the energy gaps and Altland-Zirnbauer symmetry for the system is known, the degeneracies in the parameter space are predictable [14,19,20,31,32,49]. It is thus a theoretical framework for predicting non-Hermitian topological phases of matter, providing guidance for experimental realizations. The surface of exceptional points is special, because it serves as the boundary between real and imaginary line gaps [20]. Exceptional surfaces (ES) can be commonly observed in non-Hermitian systems with parity-time inversion symmetry (*PT*) or chiral symmetry [20,25,26,27], and have broad applications in the design of sensing and absorption devices [29,48]. Two

or more ESs can intersect each other, forming stable intersection lines as a higher-order singularities, which are protected by the symmetries of the system [34,35]. Despite various important physical phenomena and potential applications, the ESs and their intersections were never topologically classified.

In this work, we consider a generic non-Hermitian  $PT$ -symmetric system with an additional pseudo-Hermitian symmetry, and such systems exhibit complete intersection lines (CIL) of ESs. By analyzing equivalence relations of eigenstates, we discovered that the quotient space of the momentum space is homotopy equivalent to “figure eight”. The topology of the structure is thus represented by the fundamental group, which is a free non-Abelian group composed of products of two generators. The topological charges in the group can be associated with the polarization conversion process of the eigenstates. Hybrid topological invariants on a closed loop circulating the intersection singularities can also be elucidated with the group structure. Besides, the conservation of topological charges systematically illustrates the variation of ESs and CILs against perturbations to the Hamiltonian.

The considered Hamiltonian is a two-level system, which is  $PT$  symmetric and preserves an additional  $\eta$ -pseudo-Hermitian symmetry [36,37]

$$[H, PT] = 0, \quad \eta H \eta^{-1} = H^\dagger \quad (1)$$

The  $PT$  operator can be regarded as a complex conjugation with a proper choice of basis, and thus the Hamiltonian can always be gauged to be real. The pseudo-Hermitian operator here takes the Riemannian metric [38,39,13] form  $\eta = \text{diag}(-1, 1)$ . It is notable that  $\eta$  is not unique: in case that the Hamiltonian performs unitary transformations,  $\eta$  transforms simultaneously (see [40] for details). The symmetries imply that the Hamiltonian can be expanded

$$H(\mathbf{k}) = f_2(\mathbf{k})i\sigma_2 + f_3(\mathbf{k})\sigma_3 \quad (2)$$

where  $f_{2,3}$  are real functions of  $\mathbf{k}$ -space, and  $\sigma_{2,3}$  are Pauli matrices. The identity can be ignored because it has no impact on the gapless structure. Such Hamiltonians correspond to physical systems with non-reciprocal hopping [41,43] of orbitals. Solving for the eigenenergies of the Hamiltonian, one discovers that the band structure shows ESs at  $f_2 = \pm f_3$ , and these surfaces intersect completely (CIL) at  $f_2 = f_3 = 0$ . The CIL is stable against perturbations to the Hamiltonian, which is a higher-order singularity compared with the ESs.

To derive the topological structure stabilizing the CIL, we firstly need to consider the gapless structure of the parameter space. Here the classification is based on the quotient space, and details on the mathematical techniques to construct quotient space are shown in Section 2 of [40]. The  $\mathbf{k}$ -space is partitioned into several regions by the ESs. As shown in Fig. 1a, the red and green lines denote ESs satisfying  $f_2 = \mp f_3$ , respectively. In regions I and III (satisfying  $|f_2| < |f_3|$ ), the eigenenergies are real, which are  $PT$ -exact phases. In contrast, regions II and IV (satisfying  $|f_2| > |f_3|$ ) are  $PT$ -broken phases, having a pair of complex-conjugate eigenenergies. It is observed that the antipodal points on ESs have the same eigenstate, which gives an equivalence relation, and the two points can be identified. A quotient space can thus be constructed by gluing antipodal points on ESs [45], forming two circular cones with their vertices coinciding and the ESs being generatrices (see Fig. 1b). The upper cone is composed of Regions I and III, and the lower cone is composed of Regions II and IV. Next, we normalize the eigenstates to be unit vectors, which corresponds a deformation retraction process of the double cone, resulting in two circles ( $S^1$ ). Antipodal points ( $f_2 \rightarrow -f_2, f_3 \rightarrow -f_3$ , see Fig. 1a) in opposite regions [i.e. region I (II) to region III (IV)] of the parameter space have the same eigenstates, and such pair of points can be identified, corresponding to the quotient of each circle  $S^1 / \mathbf{Z}_2$ , which is still  $S^1$ .

We further notice that any points on a single ES (ES<sub>1</sub> or ES<sub>2</sub>) have the same eigenstate. Hence, any point  $A$  on ES<sub>1</sub> (also any point  $B$  on ES<sub>2</sub>) can be dragged towards the common vertex of the double cone, resulting in two circles having the same base point and forming a bouquet of two circles (i.e. “figure eight”, Fig. 1c). Hence, the quotient space of the parameter space is obtained

$$M = S^1 / \mathbf{Z}_2 \vee S^1 / \mathbf{Z}_2 \cong S^1 \vee S^1 \quad (3)$$

The fundamental group can be derived as

$$\pi_1(M, A) = \mathbf{Z} * \mathbf{Z} \quad (4)$$

which is a free non-Abelian group composed of products of two generators ( $\alpha\beta \neq \beta\alpha$ ). The invariants  $\alpha$  and  $\beta$  are associated with the yellow and green paths in Fig. 1a, respectively. It is notable that these paths are open in the original parameter space, but are closed in the quotient space (yellow and green loops in Fig. 1c).

The topological invariants can be characterized by the polarization (defined by the two components of eigenstates) conversion process of eigenstates via adiabatic transformations. We first consider the exact phases (Regions I and III), the eigenstates  $\varphi_m$  ( $m=1,2$ ) are real (without arbitrary phase) and orthogonal under an indefinite inner product  $a_{mn} = \langle \varphi_m | \eta \varphi_n \rangle$  ( $a_{mn}=0$  for  $m \neq n$ ,  $a_{mn} \neq 0$  for  $m=n$ ) [36]. However, the inner products for the two eigenstates have opposite signs, revealing the Riemannian geometry [19,38,39] of the adiabatic transformation (see details in Section 3 of [40]). Hence, the polarization conversion of eigenstates is essentially induced by Lorentz boost. Along the yellow path (counter-clockwise) in Region I (Fig. 2a), the evolution processes of eigenenergies and eigenstates are shown in Fig. 2b1-b2, respectively. Here the sequence of eigenstates is defined by sorting the corresponding eigenenergies (from small to large). It is shown that the two eigenstates accumulate opposite geometric phases, inducing the polarization conversion of  $\varphi_{1,2}$  [i.e.  $\varphi'_{1,2} = \exp(\mp i\pi\sigma_2 / 2)\varphi_{1,2}$ ], respectively. The invariant  $\alpha$  can thus be characterized. If we change the sequence of the eigenstates (simultaneously the eigenenergies), the rotation angles for  $\varphi_{1,2}$  become  $\pm\pi / 2$ , corresponding to the inverse  $\alpha^{-1}$ . We note that the topological invariants are sensitive to the sequence of the eigenstates (or eigenenergies), owing to the fact that the considered system is non-Hermitian, and both options of the sequences are possible whenever a path traverses the ESs. In broken phases (regions II and IV), the eigenstates become complex, and are orthogonal under inner product  $b_{mn} = \varphi_m^T \eta \varphi_n$  ( $b_{mn}=0$  for  $m \neq n$ ,  $b_{mn} \neq 0$  for  $m=n$ ). The arbitrary phase of  $\varphi_m$  can thus be removed if we normalize the eigenstates with the inner product, and the evolution of eigenenergies and eigenstates along the green path (see Fig. 2a) is shown in Fig. 2c1-c3. It is seen that the two components of the eigenstates remain negative conjugate in the adiabatic transformation. This process converts the polarizations of eigenstates  $\varphi_{1,2}$  to the perpendicular direction, and simultaneously the two real vectors become imaginary. The rotations of  $\varphi_{1,2}$  are thus characterized by  $\mp\pi / 2$  ( $\varphi'_{1,2} = \exp(\mp i\pi\sigma_3 / 2)\varphi_{1,2}$ ), representing the invariant  $\beta$  in the group. It is shown that the invariant  $\beta$  is essentially different from  $\alpha$ , as the polarization are rotating along different axis (characterized by  $\sigma_{2,3}$  respectively). By changing the sequence of eigenstates, one also obtains the inverse invariant  $\beta^{-1}$ , similar to  $\alpha^{-1}$ . As the eigenstates cannot evolve to the initial states, both  $\alpha$  and  $\beta$  are half-integer invariants. Integer invariants can be  $\alpha^2$  or  $\beta^2$ , which is discussed in [40]. The evolutions of eigenstates along the paths in regions III and IV are the same as those in regions I and II, only the corresponding eigenenergies are swapped.

Having understood the invariants  $\alpha$  and  $\beta$ , we note that paths (or loops) carrying non-trivial topology must traverse ESs (or with terminals on ESs). A loop  $l$  without touching any ESs is confined within a specific region (see Fig. 3a), and is always trivial because it cannot enclose any singularity (or enclose several pairs of annihilable singularities). As we move the loop across the ES,  $l$  becomes a composite of two paths  $l_1$  and  $l_2$  (Fig. 2b). Such paths with two terminals on the same ES are also trivial, and eigenstates do not accumulate geometric phase along these paths. By stretching the loop to cross the other ES (see Fig. 3c),  $l$  becomes a composite of  $l_1$ - $l_4$ . Path  $l_2$  and  $l_4$  are in opposite directions (see the arrows in Fig. 3c) and have a unified sequence of eigenstates, and thus can be assigned  $\beta^{-1}$  and  $\beta$ , leading to a trivial product  $\beta^{-1}\beta=1$  ( $l_1$  and  $l_3$  are trivial). However, if one changes the sequence of eigenstates on one of the paths ( $l_2$  or  $l_4$ ), the product becomes non-trivial  $\beta^2$  or  $\beta^{-2}$ , which cannot deform to the original loop  $l$ . The non-commutativity of  $\alpha$  and  $\beta$  can be understood as follows. The invariant  $\alpha\beta$  characterizes the path that starts and ends at ES1 (red), and traverses ES2 (blue) in the middle (see Fig. 3d). However, the path for  $\beta\alpha$  is just the opposite, which starts and ends at ES2 and traverses ES1 (see Fig. 3e). A loop circulating the NIL will inevitably traverse the ESs four times, which corresponds to a composite of four paths, and its topology will have  $2^4=16$  options by considering different combinations of  $\alpha$ ,  $\beta$  and their inverses (see Table S1 in [40]). Since  $\alpha$  and  $\beta$  do not commute, these topological invariants will lead to different variation processes of eigenenergies and eigenstates. The topology on closed loops traversing ESs is well-defined only if the sequence of eigenstates is specified. To overcome the ambiguity, in the rest parts of the letter we will use the convention that the eigenstates are sorted by the corresponding eigenenergies (from small to large) in exact phases, and by the sign of imaginary parts of complex eigenenergies (from negative to positive) in broken phases. The invariant on the closed loop circulating the CIL is  $\alpha\beta\alpha^{-1}\beta^{-1}$  (counter-clockwise loop) or  $\beta\alpha\beta^{-1}\alpha^{-1}$  (clockwise loop) under this convention. It is notable that the product is not trivial, because  $\alpha$  and  $\beta$  do not commute.

With these elementary invariants taken from the group, we are able to predict the evolution of ESs and CILs as the Hamiltonian deforms. Consider the following example

$$f_2(\mathbf{k}) = k_x k_z, \quad f_3(\mathbf{k}) = -k_x^2 + k_y^2 + k_z^2 - d \quad (5)$$

The chain of CILs and ESs in  $\mathbf{k}$ -space for  $d=1$  is provided in Fig. 4a1, where the red and green surfaces denote ES<sub>1</sub> and ES<sub>2</sub> satisfying  $f_2 = -f_3$  and  $f_2 = f_3$ , respectively. We firstly look at the loop  $l_5$  in Fig. 4a1, which encloses two ESs and their intersections CILs, but does not touch any ESs. Such a loop is trivial according to our previous conclusion, which is not obvious in the figure because these ESs and CILs seemingly prevent the loop from retracting to a point. However, by changing  $d$  from positive to negative, the waists of ESs and CIL gradually retract to a point (Fig. 4b1), and finally open up to form a bandgap (Fig. 4c1). The two CILs enclosed by the loop are thus annihilable. The trivial loop  $l_5$  enforces the ESs connecting the two CILs to remain smooth as the Hamiltonian deforms. This can be explained with the loop  $l'_5$  (see Fig. 4a1). On the cross section of the plane,  $l'_5$  is segmented by ESs into several paths, as sketched in Fig. 4a2, where the red and green lines denote the ESs.  $l_5$  and  $l'_5$  are equivalent because they enclose the same CILs, and thus the invariants on the path must cancel each other to form a trivial product, meaning that the path  $l_i$  is trivial. Indeed, the starting and ending points of  $l_i$  lie on the same ES without traversing another ES. By continuing shrinking  $l'_5$ , terminal points of  $l_i$  approach CILs, and the ES between the two points must be smooth to ensure the triviality of  $l_i$ . Resultantly, as one continues to deform the Hamiltonian, the two ESs enclosed become disconnected after the two CILs annihilate (see Fig. 4c1-c2). Now we turn to  $l_6$  in Fig. 4a1, which is segmented by the ESs into different paths, and the invariant on each path is provided in Fig. 4a3. The invariant  $(\beta\alpha\beta^{-1}\alpha^{-1})^2$  on the loop also sets a constraint on the variation of the ESs inside the loop as the Hamiltonian deforms. There will always be two inannihilable CILs so that the invariant is conserved as  $d$  varies in the Hamiltonian (Eq. 5). Two CILs touches at a point at  $d=0$  (Fig. 4b1), and the nearby area is partitioned into eight regions

(see Fig. 4b3), meaning that it carries a higher invariant  $(\beta\alpha\beta^{-1}\alpha^{-1})^2$ . As one keeps varying  $d$ , the point splits, and the two CILs become isolated, as shown in Fig. 3c1 and c3. We thus understand that the invariant  $(\beta\alpha\beta^{-1}\alpha^{-1})^2$  is a necessary condition for the chain of CILs. Another condition for the presence of the chain of CILs is the mirror symmetries  $k_x \rightarrow -k_x$  and  $k_z \rightarrow -k_z$ , which will be illustrated later in the tight binding model. The conservation of the invariant also shows that two annihilable CILs cannot be connected by smooth ESs, as can be observed in Fig. 4a3-c3.

*Non-reciprocal tight binding model.* The model Hamiltonian has a simple form and can be realized with a tight binding model with non-reciprocal hoppings. A three-dimensional (3D) fcc lattice model and the corresponding Brillouin zone are shown in Fig. 5a-b, where  $M$  and  $N$  denote lattice sites. The hopping between  $M$  and  $N$  (on dark green bonds) is non-reciprocal ( $M \rightarrow N$ :  $t_1$ ,  $M \leftarrow N$ :  $-t_1$ ), and the hoppings on yellow and red bonds (between the same lattice sites but in different directions, i.e.  $M(N) \rightarrow M(N)$ :  $\vec{r}_{M(N)} \rightarrow \vec{r}_{M(N)} + \vec{a} + \vec{b}$  and  $\vec{r}_{M(N)} \rightarrow \vec{r}_{M(N)} + \vec{a} - \vec{b}$ ) are characterized by  $t_2$  and  $-t_2$ , respectively. The corresponding real space Hamiltonian is given by

$$H = \sum_{\substack{\vec{r}_M \in \vec{G}_M \\ \vec{\alpha} = \vec{a}, \vec{b}, \vec{c}}} t_1 (a_{M, \vec{r}_M}^\dagger a_{N, \vec{r}_M + \vec{\alpha}} + a_{M, \vec{r}_M}^\dagger a_{N, \vec{r}_M - \vec{\alpha}}) - h.c. + E_0 (a_{M, \vec{r}_M}^\dagger a_{M, \vec{r}_M} - a_{N, \vec{r}_N}^\dagger a_{N, \vec{r}_N}) \\ + \sum_{\substack{\vec{r}_h \in \vec{G}_h \\ h=M, N}} t_2 (a_{h, \vec{r}_h}^\dagger a_{h, \vec{r}_h + \vec{a} + \vec{b}} + a_{h, \vec{r}_h}^\dagger a_{h, \vec{r}_h - \vec{a} - \vec{b}} - a_{h, \vec{r}_h}^\dagger a_{h, \vec{r}_h + \vec{a} - \vec{b}} - a_{h, \vec{r}_h}^\dagger a_{h, \vec{r}_h - \vec{a} + \vec{b}}) \quad (6)$$

where  $E_0$  is the onsite energy of  $M$ , and  $N$  has a negative onsite energy  $-E_0$ .  $\vec{a}$ ,  $\vec{b}$  and  $\vec{c}$  are bond vectors between lattice sites  $M$  and  $N$ , and are perpendicular to each other (see Fig. 5a). The ESs and CILs for  $E_0=0$  are plotted in Fig. 5c, and the range in  $k_x$  direction is  $[0, 2\pi/d]$ , because the chain of CILs is symmetric with respect to  $\langle 1, 0, 0 \rangle$  plane (see Fig. 5b). The system has mirror symmetries  $k_x + \pi/d \rightarrow -k_x + \pi/d$  and  $k_y \rightarrow -k_y$  for  $E_0=0$ , and the invariant  $(\beta\alpha\beta^{-1}\alpha^{-1})^2$  on the orange loop ensures the presence of intersection points of CILs (black arrows). The nonzero of  $E_0$  can break the mirror symmetries in  $k_x$  and  $k_y$  directions, which eliminates the intersection points (as shown in Fig. 5d). The number of CILs inside the orange loop and the ESs traversed by the loop remain unchanged so that the invariant is conserved. The blue loop is trivial because it does not touch any ESs, and the degeneracies enclosed are waists of ESs (see Fig. 5c-d), independent of the mirror symmetries. The variation of ESs and CILs in lattice models is consistent with our predictions.

In summary, we topologically classified a generic non-Hermitian two-level system with  $PT$  symmetry and an additional pseudo-Hermitian symmetry, corresponding to systems with non-reciprocal hoppings [46,47,44]. Such systems exhibit surfaces of exceptional points, which intersect stably in momentum space. We showed that the topology of such gapless structure can be viewed from its quotient space, which is a bouquet of two circles, and its fundamental group is isomorphic to a free non-Abelian group with two generators. Elementary invariants in the group are associated with the adiabatic transformations of eigenstates. Hybrid topological invariant on a closed loop circulating an intersection singularity is revealed from the group, and the group structure allows the prediction of the variation of ESs and CILs as the Hamiltonian deforms. Our classification is a global topological description and does not rely on specific bandgaps. The method of quotient space topology might potentially be extended to classify other intersection or cusp singularities, such as high-order exceptional points [30,48]. Our work predicts a new topological phase of matter, providing pathways for designing systems

to realize robust topological phases. The classification also provides guidance for the design of relevant devices in sensing and lasing applications using exceptional surfaces and their intersections.

#### References:

1. Lu L, Fu L, Joannopoulos J D, et al. Weyl points and line nodes in gyroid photonic crystals[J]. *Nature photonics*, 2013, 7(4): 294-299.
2. Lu L, Joannopoulos J D, Soljačić M. Topological photonics[J]. *Nature photonics*, 2014, 8(11): 821-829.
3. Abanin D A, Morozov S V, Ponomarenko L A, et al. Giant nonlocality near the Dirac point in graphene[J]. *Science*, 2011, 332(6027): 328-330.
4. Jiang Z, Zhang Y, Stormer H L, et al. Quantum Hall states near the charge-neutral Dirac point in graphene[J]. *Physical review letters*, 2007, 99(10): 106802.
5. Lu L, Wang Z, Ye D, et al. Experimental observation of Weyl points[J]. *Science*, 2015, 349(6248): 622-624.
6. Wu Q S, Soluyanov A A, Bzdušek T. Non-Abelian band topology in noninteracting metals[J]. *Science*, 2019, 365(6459): 1273-1277.
7. Yang E, Yang B, You O, et al. Observation of non-Abelian nodal links in photonics[J]. *Physical Review Letters*, 2020, 125(3): 033901.
8. Guo Q, Jiang T, Zhang R Y, et al. Experimental observation of non-Abelian topological charges and edge states[J]. *Nature*, 2021, 594(7862): 195-200.
9. Soluyanov A A, Gresch D, Wang Z, et al. Type-ii Weyl semimetals[J]. *Nature*, 2015, 527(7579): 495-498.
10. Yang L X, Liu Z K, Sun Y, et al. Weyl semimetal phase in the non-centrosymmetric compound TaAs[J]. *Nature physics*, 2015, 11(9): 728-732.
11. Yang B, Guo Q, Tremain B, et al. Ideal Weyl points and helicoid surface states in artificial photonic crystal structures[J]. *Science*, 2018, 359(6379): 1013-1016.
12. Jia H, Zhang R, Gao W, et al. Observation of chiral zero mode in inhomogeneous three-dimensional Weyl metamaterials[J]. *Science*, 2019, 363(6423): 148-151.
13. Jia H, Zhang R Y, Gao W, et al. Chiral transport of pseudospinors induced by synthetic gravitational field in photonic Weyl metamaterials[J]. *Physical Review B*, 2021, 104(4): 045132.
14. Gong Z, Ashida Y, Kawabata K, et al. Topological phases of non-Hermitian systems[J]. *Physical Review X*, 2018, 8(3): 031079.
15. Yao S, Wang Z. Edge states and topological invariants of non-Hermitian systems[J]. *Physical review letters*, 2018, 121(8): 086803.
16. Shen H, Zhen B, Fu L. Topological band theory for non-Hermitian Hamiltonians[J]. *Physical review letters*, 2018, 120(14): 146402.
17. Okuma N, Kawabata K, Shiozaki K, et al. Topological origin of non-Hermitian skin effects[J]. *Physical review letters*, 2020, 124(8): 086801.

18. Leykam D, Bliokh K Y, Huang C, et al. Edge modes, degeneracies, and topological numbers in non-Hermitian systems[J]. Physical review letters, 2017, 118(4): 040401.
19. Bergholtz E J, Budich J C, Kunst F K. Exceptional topology of non-Hermitian systems[J]. Reviews of Modern Physics, 2021, 93(1): 015005.
20. Kawabata K, Shiozaki K, Ueda M, et al. Symmetry and topology in non-Hermitian physics[J]. Physical Review X, 2019, 9(4): 041015.
21. Borgnia D S, Kruchkov A J, Slager R J. Non-Hermitian boundary modes and topology[J]. Physical review letters, 2020, 124(5): 056802.
22. Kawabata K, Bessho T, Sato M. Classification of exceptional points and non-Hermitian topological semimetals[J]. Physical review letters, 2019, 123(6): 066405.
23. Song F, Yao S, Wang Z. Non-Hermitian topological invariants in real space[J]. Physical review letters, 2019, 123(24): 246801.
24. Zhou H, Peng C, Yoon Y, et al. Observation of bulk Fermi arc and polarization half charge from paired exceptional points[J]. Science, 2018, 359(6379): 1009-1012.
25. Zhou H, Lee J Y, Liu S, et al. Exceptional surfaces in PT-symmetric non-Hermitian photonic systems[J]. Optica, 2019, 6(2): 190-193.
26. Okugawa R, Yokoyama T. Topological exceptional surfaces in non-Hermitian systems with parity-time and parity-particle-hole symmetries[J]. Physical Review B, 2019, 99(4): 041202.
27. Zhang X, Ding K, Zhou X, et al. Experimental observation of an exceptional surface in synthetic dimensions with magnon polaritons[J]. Physical review letters, 2019, 123(23): 237202.
28. Yang Z, Hu J. Non-Hermitian Hopf-link exceptional line semimetals[J]. Physical Review B, 2019, 99(8): 081102.
29. Zhong Q, Ren J, Khajavikhan M, et al. Sensing with exceptional surfaces in order to combine sensitivity with robustness[J]. Physical review letters, 2019, 122(15): 153902.
30. Tang W, Jiang X, Ding K, et al. Exceptional nexus with a hybrid topological invariant[J]. Science, 2020, 370(6520): 1077-1080.
31. Wojcik, Charles C., et al. "Homotopy characterization of non-Hermitian Hamiltonians." Physical Review B 101.20 (2020): 205417.
32. Sun X Q, Wojcik C C, Fan S, et al. Alice strings in non-Hermitian systems[J]. Physical Review Research, 2020, 2(2): 023226.
34. Miri M A, Alu A. Exceptional points in optics and photonics[J]. Science, 2019, 363(6422).
35. Özdemir Ş K, Rotter S, Nori F, et al. Parity–time symmetry and exceptional points in photonics[J]. Nature materials, 2019, 18(8): 783-798.
36. Mostafazadeh A. Pseudo-Hermitian representation of quantum mechanics[J]. International Journal of Geometric Methods in Modern Physics, 2010, 7(07): 1191-1306.
37. Mostafazadeh A. Quantum brachistochrone problem and the geometry of the state space in pseudo-Hermitian quantum mechanics[J]. Physical review letters, 2007, 99(13): 130502.
38. Freedman D Z, Van Proeyen A. Supergravity[M]. Cambridge university press, 2012.
39. Frankel T. The geometry of physics: an introduction[M]. Cambridge university press, 2011.

40. supplementary material
41. Helbig T, Hofmann T, Imhof S, et al. Generalized bulk–boundary correspondence in non-Hermitian topoelectrical circuits[J]. *Nature Physics*, 2020, 16(7): 747-750.
42. Wang X, Ptitsyn G, Asadchy V S, et al. Nonreciprocity in bianisotropic systems with uniform time modulation[J]. *Physical Review Letters*, 2020, 125(26): 266102.
43. Ezawa M. Non-Hermitian non-Abelian topological insulators with PT symmetry[J]. *Physical Review Research*, 2021, 3(4): 043006.
44. Buddhiraju S, Song A, Papadakis G T, et al. Nonreciprocal metamaterial obeying time-reversal symmetry[J]. *Physical Review Letters*, 2020, 124(25): 257403.
45. Spanier E H. *Algebraic topology*[M]. Springer Science & Business Media, 1989.
46. Floess D, Chin J Y, Kawatani A, et al. Tunable and switchable polarization rotation with non-reciprocal plasmonic thin films at designated wavelengths[J]. *Light: Science & Applications*, 2015, 4(5): e284-e284.
47. Delplace P, Yoshida T, Hatsugai Y. Symmetry-protected multifold exceptional points and their topological characterization[J]. *Physical review letters*, 2021, 127(18): 186602.
48. Soleymani S, Zhong Q, Mokim M, et al. Chiral coherent perfect absorption on exceptional surfaces[J]. *arXiv preprint arXiv:2107.06019*, 2021.
49. Li Z, Mong R S K. Homotopical characterization of non-Hermitian band structures[J]. *Physical Review B*, 2021, 103(15): 155129.



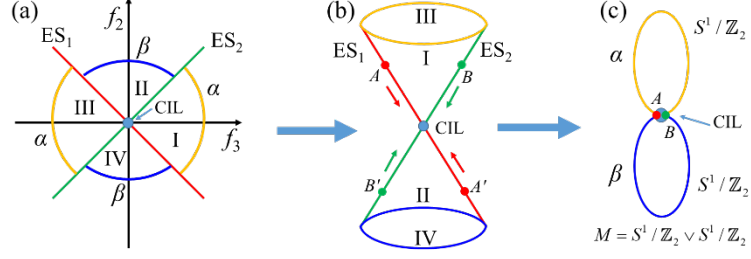


Fig. 1. Construction of quotient space under equivalence relations. (a) The gapless structure of original parameter space,  $ES_{1,2}$  characterize exceptional surfaces satisfying  $f_2 = \mp f_3$ , respectively. Regions I and III are  $PT$ -exact phases with real line gaps, and Regions II and IV are  $PT$ -broken phases with imaginary line gaps. The ESs intersect (CIL) at  $f_2=f_3=0$ . (b) Identifying antipodal points on ESs gives a quotient space, which is a double cone with a common vertex. (c) By normalizing the eigenstates to be unit vectors, the double cone deformation retracts to two circles ( $S^1$ ). Antipodal points in opposite regions correspond to a pair of point on a  $S^1$ , and the two points have the same eigenstates and can be identified ( $S^1 / \mathbb{Z}_2$ ). All points on a single ES have the same eigenstates and can be dragged towards the center. The final quotient space of “figure eight” can be constructed.

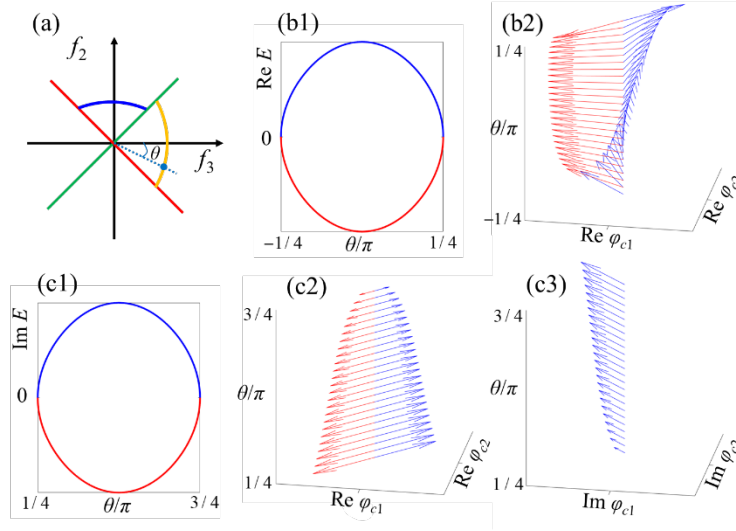


Fig. 2. Characterizing topological invariants  $\alpha$  and  $\beta$  with polarization conversion of eigenstates. (a) Setting  $f_3 = \cos\theta$ ,  $f_2 = \sin\theta$ , the yellow loop in region I is in the interval  $\theta \in [-\pi/4, \pi/4]$ , and the blue loop in region II is in  $\theta \in [\pi/4, 3\pi/4]$ . (b1-c1) Evolution of eigenenergies along the two paths, respectively (Fig. 1a, counter-clockwise). (a2, b2-b3) Polarization conversion of eigenstates along the paths induced by adiabatic transformations, corresponding to invariants  $\alpha$  and  $\beta$ , respectively.  $\varphi_{c1}$  and  $\varphi_{c2}$  are the components of the eigenstates, and Re and Im denote real and imaginary parts, respectively. Blue and red lines (arrows) correspond to  $E_1$  ( $\varphi_1$ ) and  $E_2$  ( $\varphi_2$ ) in (b-c), respectively.

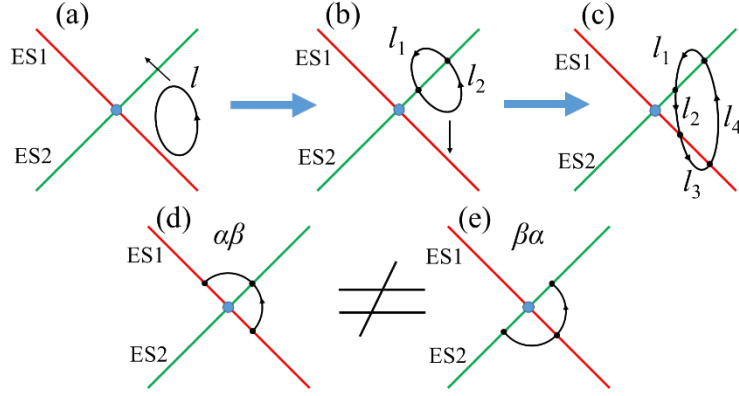


Fig. 3. Trivial loops and non-commutativity of  $\alpha$  and  $\beta$ . (a) A loop without touching ESs is confined within a specific region and is trivial. (b) Moving the loop along the black arrow direction (see (a)), the loop becomes a composite of paths  $l_1$  and  $l_2$ . Both of  $l_1$  and  $l_2$  are trivial, and their composite loop is also trivial. (c) Stretching the loop along the black arrow direction in (b), the loop crosses ES1 and becomes a composite of  $l_1$ - $l_4$ . The invariants on paths  $l_2$  and  $l_4$  can cancel each other by fixing the sequence of eigenstates, and the composite loop is still trivial. (d-e) paths characterizing non-trivial invariants  $\alpha\beta$  and  $\beta\alpha$ , respectively. The two paths are inequivalent to each other because their starting and ending points are on different ESs. The ESs traversed by the paths are also different.

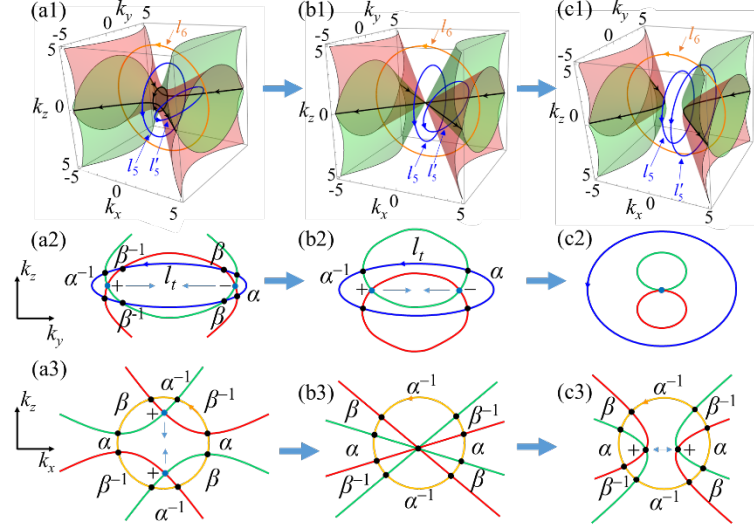


Fig. 4. Evolution of ESs and CILs against perturbations to the Hamiltonian. (a1-c1) ESs (red and green surfaces) and CILs (black lines) plotted with Eq. 5, corresponding to  $d > 0$ ,  $d = 0$  and  $d < 0$ , respectively. The blue loops  $l_5$  and  $l'_5$  have trivial topological charges. (a2-c2) Cross section of the plane that  $l'_5$  locates on. The enclosed pair of CILs can annihilate each other. (a3-c3) Cross section of the plane that the orange  $l_6$  locates on. The CILs enclosed cannot annihilate each other. Red and green lines: ESs; Dark blue dots: CILs; Black dots: intersecting points of loops on ESs (in Row 2 and Row 3).

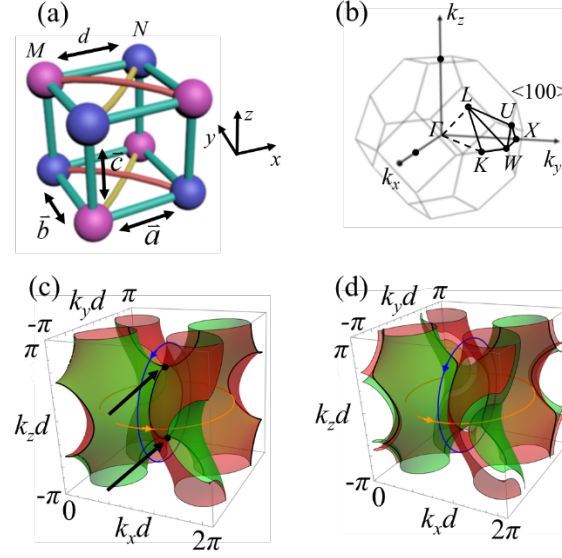


Fig. 5. Proposal of an fcc lattice model with non-reciprocal hoppings. (a) fcc lattice with two sites  $M$  (blue balls) and  $N$  (pink balls). The interspace distance between  $M$  and  $N$  is  $d$ , and  $\vec{a}$ ,  $\vec{b}$  and  $\vec{c}$  are bond vectors. The hopping on dark green bonds is non-reciprocal ( $M \rightarrow N$ :  $t_1$ ,  $M \leftarrow N$ :  $-t_1$ ). The hopping on the same lattice sites in different directions (in  $\vec{a} + \vec{b}$  and  $\vec{a} - \vec{b}$ ) have opposite signs (hopping on yellow bonds:  $t_2$ , hopping on red bonds:  $-t_2$ ). (b) First Brillouin zone of the fcc lattice. (c-d) ESs (red and green surfaces) and CILs (black lines) for  $E_0=0$  and  $E_0 \neq 0$  in Eq. 6. (c) has a chain of CILs, which is symmetric with respect to  $\langle 100 \rangle$  plane. The intersecting points on the chain are labelled with black arrows.